Nanoscale Advances

ROYAL SOCIETY OF CHEMISTRY

PAPER

View Article Online
View Journal | View Issue

Cite this: *Nanoscale Adv.*, 2025, **7**, 2322

A dynamic broadband plasmonic absorber enabled by electrochemical lithium metal batteries†

Huiling Yu *

As plasmonic absorbers attract considerable attention in the fields of solar energy harvesting, sensors, and cloaking technology, achieving dynamic tuning holds promise for multifunctional applications. However, existing designs face challenges in achieving real-time dynamic regulation across the visible band. In this study, we propose an innovative approach to achieve dynamic broadband absorption at visible wavelengths *via* an electrochemical lithium metal battery. Through rigorous experimentation and simulation, we demonstrate that the dynamic absorber achieves remarkable reversibility, with 80% absorption at lithium deposition states and a 40% modulation amplitude in reflectance over 30 cycles. At the intersection of the plasmonic absorber and lithium battery, our results may provide insights for light detection such as the monitoring environment.

Received 18th November 2024
Accepted 22nd February 2025

DOI: 10.1039/d4na00950a

rsc.li/nanoscale-advances

1 Introduction

Metamaterials exhibit extraordinary electromagnetic properties owing to their tailored geometric structures or dimensions, allowing them to capture or modulate optical fields effectively. A broadband absorber is one of the most rapidly advancing areas in this field, presenting optimal applications in solar energy harvesting,[1–5] thermal emitters,[6–9] sensors,[10–12] and cloaking.[13–16] Currently, broadband absorbers employ multilayered structures composed of metal and dielectric layers[5,17–19] or high-loss metal materials,[7,20] which are limited in application to single or multiple frequency bands for optical detection and sensing. Moreover, most absorbers remain static with fixed optical properties and a restricted range of spectral regulation.[20–23]

To meet the escalating demand for electromagnetic applications, dynamic metamaterial broadband absorbers are needed. Researchers have explored different design strategies using phase change materials to achieve dynamic broadband absorbers.[24] Materials, such as VO_2 (ref. 25 and 26) and $Ge_2Sb_2Te_5$,[27,28] undergo reversible phase transition triggered by external stimuli, which regulate their absorption properties. However, their optical responses are discrete, which are only transformed between two states with a low degree of tunable freedom, and lacks a full-band tunability within visible light (400–780 nm). Consequently, there is a pressing need to develop a dynamic absorber for continuous and adjustable absorption modulation across this broad visible spectral range.

Dynamic plasmonics—also known as reconfigurable or programmable plasmonics—enables active tuning of plasmonic structures and their optical responses using external fields. Various strategies have been proposed, including electrical controls,[29,30] thermal stimuli,[31,32] and mechanical strains.[33,34] Electrochemically driven dynamic plasmonics stands out as a hybrid method that combines electrical control with chemical reactions, offering flexible on-chip integration and a wide range of chemical transformations for diverse applications. A key example of structural transformation is metal deposition and stripping, which involves electrochemical deposition followed by removal through reduction and oxidation. However, most electrochemical dynamic plasmonic systems currently focus on noble metal structures, such as gold and silver.

Fortunately, plasmonic absorbers have shown great potential to achieve high absorptivity in the visible and infrared regions owing to their diverse nanostructures and metallic materials.[5,35–38] Absorption in plasmonic absorbers is enhanced through mechanisms such as localized surface plasmons, surface plasmon polaritons, and magnetic plasmons.[10,37,39,40] Compared to noble metals like gold and silver, alkali metals are considered as ideal plasmonic materials owing to their lower optical loss and cost.[41] Recent research has shown that absorption or reflectance can be tuned by altering the structures of plasmonic materials, enabling high integration and low energy consumption.[20,22,42] Although dynamic alkali plasmons[43–45] have primarily focused on the visible and near-infrared wave bands, achieving dynamic broadband absorption in the visible spectrum remains a challenge.

In this study, we introduce an innovative broadband dynamic plasmonic absorber that operates electrochemically in the full-spectrum visible region. The design of this dynamic absorber, which is based on a Li metal battery, achieves

National Laboratory of Solid State Microstructures, College of Engineering and Applied Sciences, Nanjing University, Nanjing, Jiangsu 210023, P. R. China. E-mail: MF20340078@smail.nju.edu.cn

† Electronic supplementary information (ESI) available. See DOI: https://doi.org/10.1039/d4na00950a

continuous broadband absorption modulation (with 80% absorption at lithium deposition states and 40% reflectance modulation amplitude) through the electrochemical deposition and stripping of Li metal during charging and discharging. Besides, the absorber shows great reversibility over 30 cycles. Our research provides a new direction of modulation strategy for optical detection.

2 Results and discussion

2.1 Design principle of the dynamic broadband plasmonic absorber based on a lithium metal battery

The proposed dynamic broadband absorber relies on the structure transformation of plasmonic materials through the electrochemical process in a planar Li metal battery (see Method for detailed information), as depicted in Fig. 1. The absorption of visible light can be tuned by selectively depositing and stripping Li metal particles on Au seeds. To validate the regulated absorber across 400 to 800 nm, two essential elements are required. First, electrochemical processes drive reversible structural transformations across the visible wavelengths. Second, the plasmonic material should possess optical resonance excitations across visible wavelengths. In this study, we prepared a randomly distributed Au nanoparticle on tungsten substrate, inducing selective deposition and stripping of lithium metal. Au is chosen as the Li nucleation seeds considering its smaller nucleation overpotential compared to substrate W metals. Upon applying a suitable current density, Li ions from the positive electrode migrate to the Au sites, initiating selective Li metal deposition and consequent continuous growth of Li particles. The randomness and continuity in diameters and distributions (upper panel in Fig. 1) induce hybrid plasmon resonances.

The validation is conducted on a planar battery. The planar battery we designed differs significantly from conventional coin cells in three main aspects: its transparent design that allows light to enter, the absence of a separator due to the increased distance between electrodes, and the longer distance between the electrodes. Generally, the current density is higher near the electrodes and relatively lower in the middle region. However, in this battery, the increased distance may result in a more uniform current density, which is beneficial for the deposition and dissolution of metallic lithium. Unlike coin cells, where the current density may be higher in the central region, the planar battery maintains a relatively uniform current density across its surface, which might facilitate controlled lithium metal deposition and dissolution.

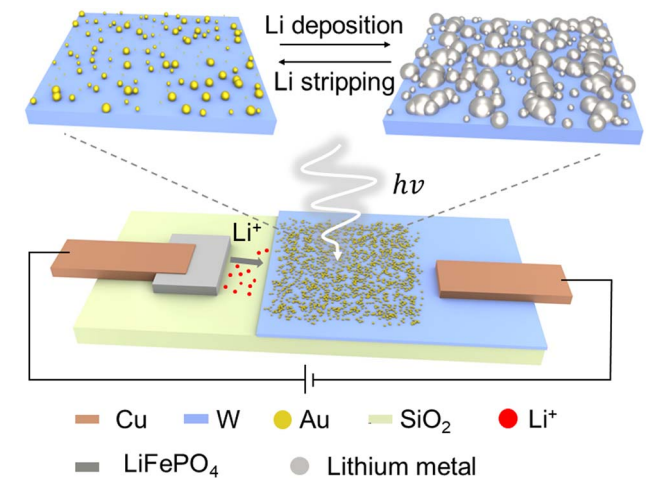

Fig. 1 The schematic of the dynamic broadband plasmonic absorber *via* selective lithium deposition and stripping in an electrochemical lithium metal battery.

In the battery, when the external constant current is applied, the reduction and oxidation reactions of lithium metal occur. When the battery is charged, lithium ions exit from the positive electrode into the negative electrode, due to the lipophilicity of gold, resulting in lithium and gold reaction directionally, then the formation of lithium gold alloy, and finally nucleation and growth of Li metal at this time corresponding to enhanced light absorption. Similarly, when the battery is discharged, the lithium metal dissolves, the lithium metal hemispheres become smaller, and finally the dealloying reaction occurs, and at the same time, the absorption is weakened. In this regulation process, the transformation process of the lithium metal structure is the key point in the real-time monitoring method, which is important for optical detection.

Then, we calculated the optical responses of the gold substrate and Li metal nanoparticles (NPs) in different stages, as illustrated in the upper panel of Fig. 1, through the finite-difference time domain (FDTD) (see Methods for details). The reflectance of a gold nanoparticle substrate, with an average diameter (d) of ~10 nm, exceeds 90% across the 400–800 nm visible range, as shown in the black curve in Fig. 2a. Once Li ions start to deposit on the gold sites, the reflectance is reduced as the diameter of lithium particles increased. At a lithium nanoparticle diameter of 100 nm, the reflectance is reduced from 90% to 60%. With further Li deposition, the reflectance reduces from 60% to 30% as the lithium particle reaches 200 nm, indicating a high degree of modulation for absorption. The reflectance (R) is derived from simulation, and the absorption (A) is calculated according to the following equation:

$$A = 1 - R - T \quad (1)$$

where T denotes transmittance. During the charging and discharging process, the continuous changes of Li NPs lead to dynamic absorption.

Besides, the extinction cross-section of a single Li metal particle with various d is simulated in Fig. 2b. Large-sized Li metal particles (after Li deposition) can generate stronger plasmonic absorption toward the visible region, which illustrates that the incident light can be localized around the NPs, thereby reducing the reflection efficiency. The larger the individual Li particle (d increases discretely from ~10 nm to ~500 nm), the more prominent and wider the localized surface plasmon (LSP) resonance mode becomes.

In addition to the LSP for a single Li particle, surface plasmon coupling between two or more Li particles can further enhance visible light absorption. As shown in Fig. 2c–e, the electric field distribution for multiple Li particles in the

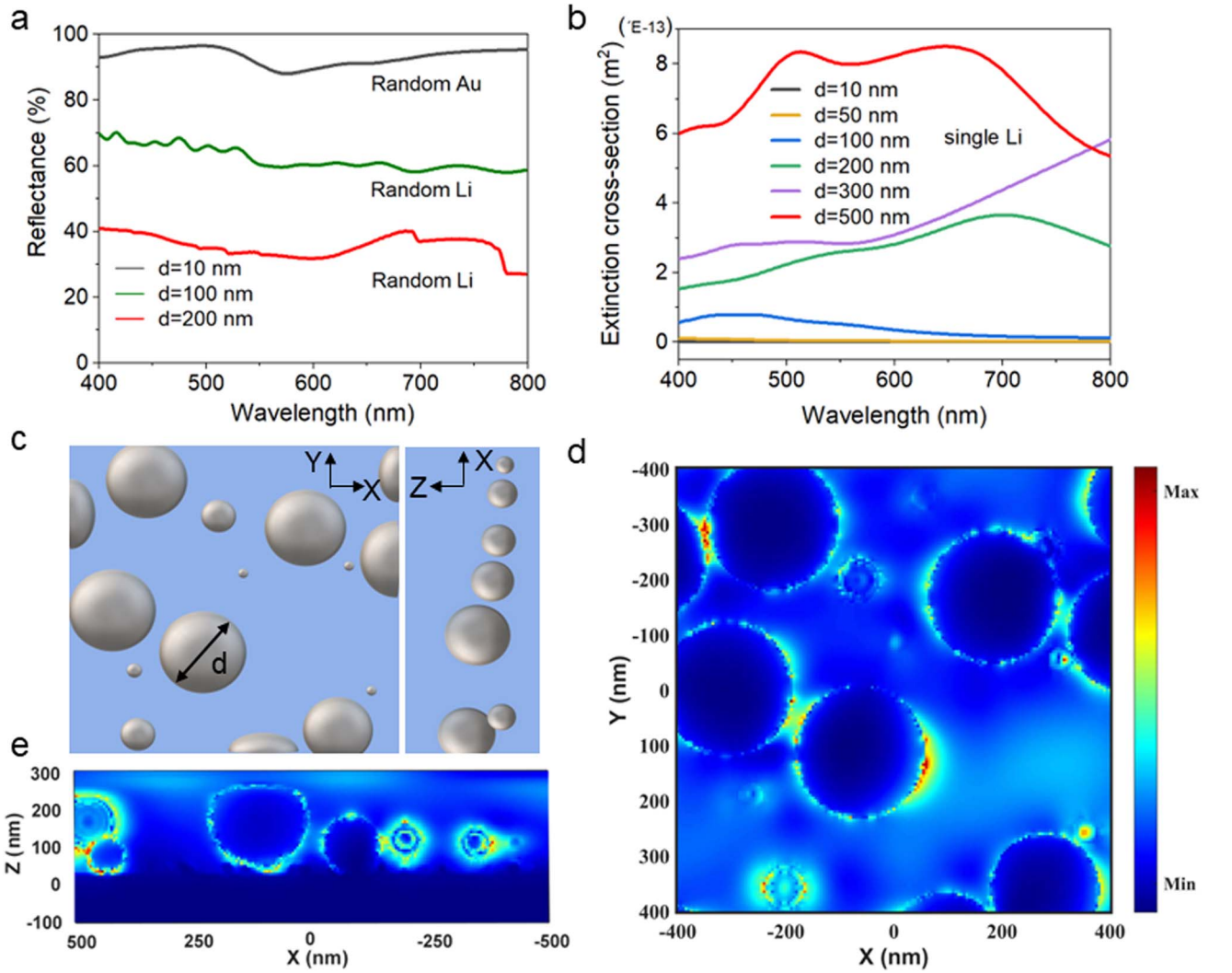

Fig. 2 Simulated reflectance and electric field distribution of the lithium nanoparticles. (a) Simulated reflectance of random Au and Li particles. (b) The simulated extinction cross-section of a single Li particle with different d (diameter). (c) The schematic diagram of random lithium particles, and (d) the simulated electric field distribution of the *XY* plane at $\lambda = 605$ nm, and (e) the simulated electric field distribution of the *XZ* plane at $\lambda = 605$ nm.

randomness of the *XY*- and *XZ*-planes at a wavelength of 605 nm demonstrates strong LSP and plasmonic coupling resonances among random Li particles with varying *d*. In particular, the electric field is enhanced as particles get closer. Thus, the spacing distance plays a key role in the field distribution. Following Li deposition, a hybrid resonance mode occurs as the diameter of Li NPs increases and the spacing distance between them decreases. Therefore, the hybrid optical mode broadens absorption and reduces reflectance across the 400–800 nm region. Furthermore, after Li stripping, the diameter of lithium particles decreases and the spacing distance gradually increases, weakening the resonance intensity, leading to a decrease in absorption and an increase in reflectance.

2.2 Electrochemical tunability of the broadband plasmonic absorber

We further validate the absorber design by experiment. To achieve the dynamic absorber, the Au structure is firstly prepared as a negative electrode *via* the sputtering-annealing method (see ESI, Section 1, and Fig. S1, S2† for details), which is simple and economical. The high-resolution scanning electron microscopy (SEM) image reveals that the average diameter distribution of gold NPs is approximately 15 nm, as shown in Fig. S4.† Before lithium deposition, we performed *ex situ* reflectance measurement of the Au structure in the battery assembled with the electrolyte, as shown in Fig. S3.† The reflectance profile is consistent with the simulated profile, indicating that the Au structure is suitable for inducing Li deposition.

The morphology of Li metal NPs plays a crucial role in tuning the absorption of visible light. To estimate the absorption tunability of the visible broadband absorber, *in situ* reflectance tests were conducted (an optical microscope, a spectrometer, an electrochemical workstation and a laptop work simultaneously) during the entire process of lithium metal deposition and stripping, as illustrated in Fig. 3, which can reveal the

relationship between the Li morphology and reflection spectrum in the visible bandwidth. Essentially, the absorber is a planar battery with an optical window, which allows light to pass through the upper surface to reach the reactive substrate. Moreover, the Au substrate dominates the morphology of Li metal particles. The voltage and current density are presented in Fig. 3a and b, respectively. The growth of Li particles is driven by constant currents (charging at 0.125 mA cm^{-2} and discharging at 0.0625 mA cm^{-2}), as plotted in Fig. 3b. External electrical stimulation is necessary for this absorber to work. Li begins to deposit after an electrical current is applied, and the *in situ* spectral evolution tendency is presented in Fig. 3c. As the charging time increases, Li metal is deposited at gold sites and the diameter increases, thereby enhancing the absorption, shown in reflectance lines at 100 s and 140 s. After 170 s, the initial 90% reflectance decreases stepwise to 50%. The reflectance spectra remain flat across 400 to 800 nm without any clear peak and have uniform absorption across the visible range. Similarly, in the lithium stripping process, the reflectance returns to ~80% in the fully visible region, presented in Fig. 3d. These experimental reflectance results can be attributed to the evolved growth of Li particles, which may cause the fusion of adjacent particles[46] and variations in the Li morphology to realize broadband absorption. This tuning capability enables the device to operate under specific environments or conditions, enhancing its dynamic detection capabilities and flexibility. The SEM images presented in Fig. 3f further validate that the random Li particles are composed of different diameters. Lastly, Fig. 3g shows that the substrate maintains its original reflectance, with only a slight change (compared with the original one in Fig. 3e) in the size of the Au substrate owing to the incomplete removal of Li metal. The tunability allows the absorber device to respond to external changes and adapt to different detection conditions, obtaining real-time data.

To further unveil the continuity of reflectance regulation in the absorber, we present the continuous reflectance diagram

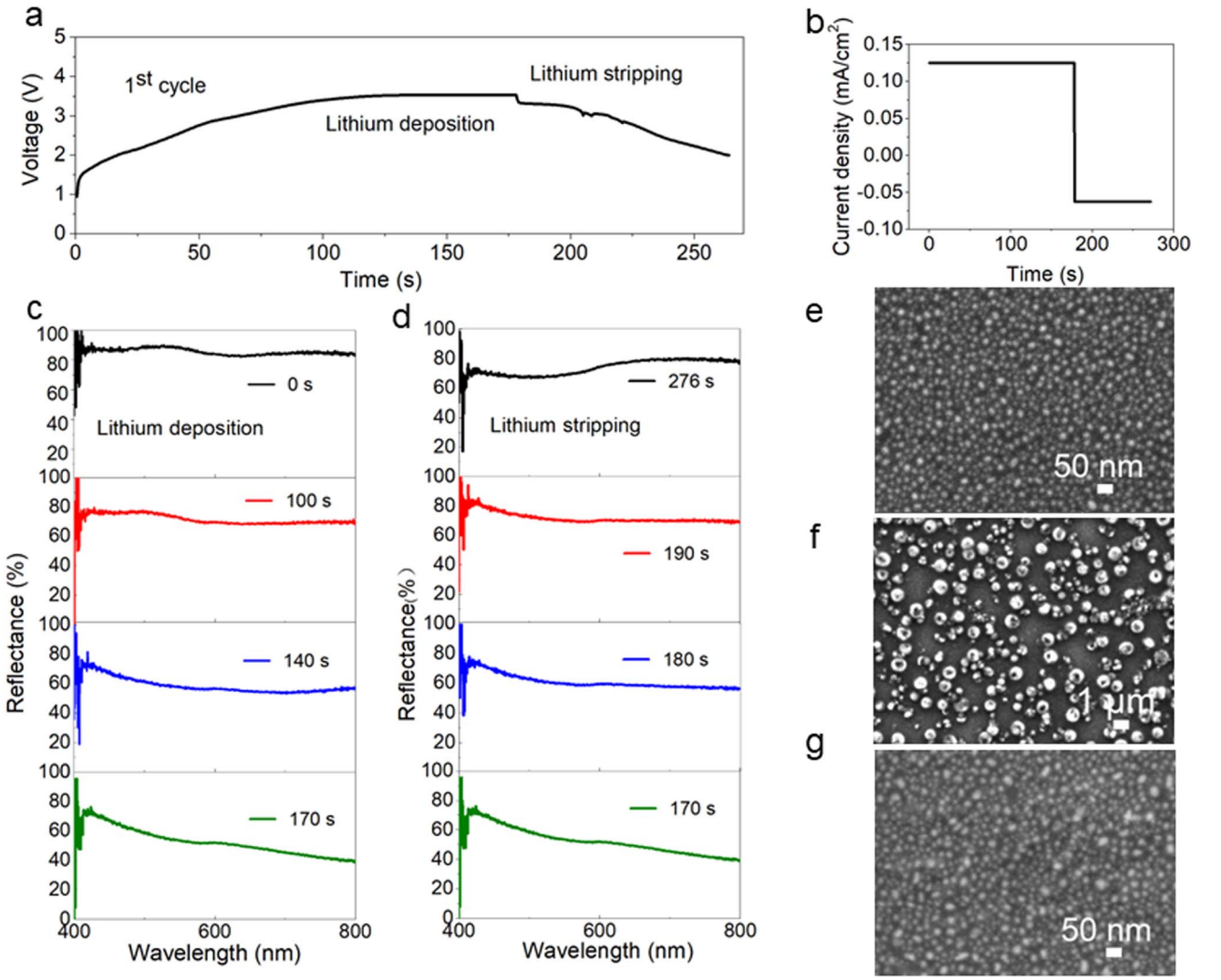

Fig. 3 *In situ* reflectance and SEM characterization of disorder Li structure during the first cycling. (a) Battery voltage curve of the first cycle. (b) The battery current density profile in the first charging and discharging process. (c) *In situ* reflectance spectrum during lithium deposition. (d) *In situ* reflectance spectrum during lithium stripping. (e–g) SEM images of the absorber at stages of the (e) original, (f) Li particle generation and (g) Li stripping states during the first cycle.

over cycling. The reflectance follows the same profile at any response time as shown in Fig. S5.† Due to different *d* of Li particles, the modes of LSP and multi-particle coupling resonance coexist, allowing the absorber to achieve broadband resonance. Conversely, the stepwise transformation of Li metal morphology during cycling results in continuous reflectance and tunability.

2.3 Cycling performance of the dynamic absorber

The cycling stability of tuning absorption is an important parameter. The absorber was subjected to continuous electrochemical cycle tests for 30 cycles under the same conditions of current and amplitude. Reflectance amplitude is defined as the difference in reflectance between the original state and the end-of-charge state. Fig. 4a–c show the *in situ* reflectance characterization in three states during Li structure transformation (original state, end of charging state, end of discharging state) at three wavelengths of 450 nm, 600 nm and 800 nm. At 450 nm, the original reflectance value is 90% and gradually stabilizes at approximately 60% as the number of cycles increases (specifically from the sixth cycle, after which the Au substrate gets more stable), as shown in the black curve in Fig. 4a. During cycling, Au particles expand and shrink. When the diameters of the Li particles reach their maximum at the end of the charging state, the reflectance remains constant at approximately 20% (maximum absorption in this state), as indicated by the red line in Fig. 4a. Reflectance between 20% and 90% shows that it can work in weak light intensity. The reflectance curve for the initial state exhibits a similar trend to that of the fully charged state, eventually reaching a steady level, as shown in Fig. 4a. Additionally, after the sixth cycle, the reflectivity at the end of the discharge state is close to the value in the initial state across the entire spectrum of 400–800 nm, as illustrated by the blue lines in Fig. 4a. Notably, the reflectance consistently achieves a modulation amplitude of 40% in each cycle.

Similarly, the change trend of reflectance and amplitude at wavelengths of 600 nm and 800 nm, as shown in Fig. 4b and c, maintains 40% modulation amplitude of reflectivity through the fully visible region within 30 cycles. This means that the device can effectively capture and utilize light signals without measurement consistency being affected by changes in wavelength. During the initial phase of the reaction, gold nanoparticles react with Li to form a Li–Au alloy, which facilitates uniform deposition and stripping of Li metal.[40] Concurrently, exposure of Li metal to the electrolyte leads to the formation of a solid electrolyte interface layer, which prevents further reaction of Li metal with the electrolyte and stabilizes the substrate. During discharging, the Li–Au alloy may be inadequately stripped, resulting in the enlargement of gold particles to change the original reflectance. During the first 6 cycles, the reflectance at the end of the discharge state is lower than the initial state, as depicted in Fig. 4a–c. Once the gold structure is stabilized after several cycles, the reflectance returns to its original value and remains consistent.

The morphology of the deposition substrate plays a role in the cycling performance of the absorber. Fig. 4d–f show the gold structure morphology after the 2nd, 15th, and 25th cycles. It is evident that the gold morphology remains a random arrangement of grains. In the 15th cycle, the sizes of gold particles focus on 20 nm and absorption is distributed across the entire visible

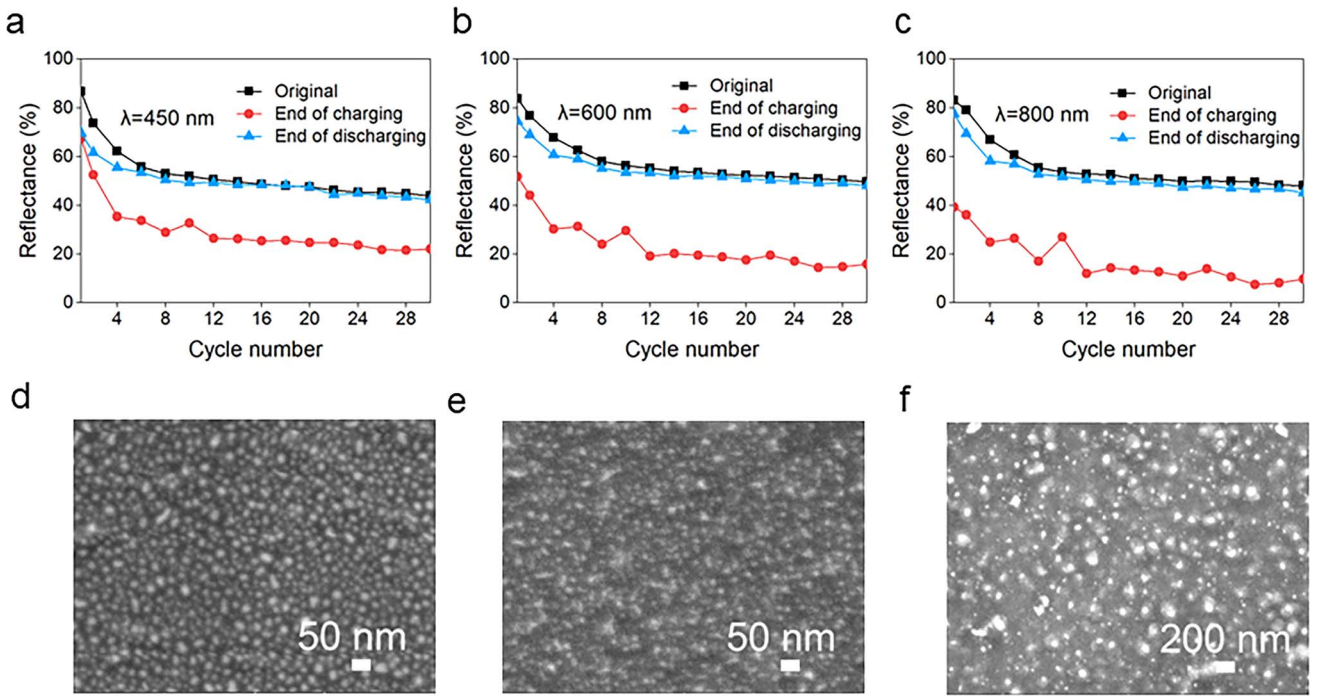

Fig. 4 Cycling performance of the absorber. (a–c) *In situ* reflectance spectrum corresponding to three states (original, end of charge, end of discharge) at different wavelengths ((a) $\lambda = 450$ nm, (b) $\lambda = 600$ nm, (c) $\lambda = 800$ nm) during cycling. (d–f) SEM images of the anode after the 2nd cycle, the 15th cycle and the 25th cycle.

light in Fig. S6,† indicating that the substrate shows good reversibility. After 25 cycles, the gold particles still exist with increased diameters in Fig. 4f (see the reflectance performance in ESI Fig. S7† for details). Therefore, the stability of the gold substrate is a crucial factor in determining cycling performance for the dynamic broadband absorber in the case of 40% reflectance amplitude.

3 Conclusion

In conclusion, our study successfully demonstrates a dynamic plasmonic broadband absorber in the entire visible region, enabled by an electrochemical Li metal battery. During the battery charging and discharging process, the random lithium particles are selectively deposited on Au nucleation seeds (an Economical method) and stripped out, leading to the tunability of broadband reflectance because of the LSP effect of individual Li particles and the coupling resonance of multiple particles, revealed by numerical simulations and *in situ* experiment. The dynamic absorber demonstrates remarkable reversibility for 30 cycles, with 80% absorption at the lithium deposition state and 40% reflectance change per cycle. The tunability and broadband absorption in the visible region enhance the sensitivity and allow for real-time adjustments of its absorption properties by altering the structures of Li metal nanoparticles. It is expected to be applied in optical sensing and detection such as detecting environmental light and being integrated with other optical systems to increase functionality.

In future applications, wider angle range, wider wavelengths such as the near-infrared range, and fast response speed should be considered to detect light from various environments. In the following research, performances and practical application operations should be further improved from two aspects in material substrates and structural improvements to broaden the scope of application.

4 Experimental methods

4.1 Numerical simulation

The Finite-Difference Time-Domain (FDTD Solutions V8.6) is mainly used to calculate the reflection spectrum of randomly deposited lithium nanoparticles, the absorption cross-section and the scattering cross-section of a single lithium nanoparticle. The light source wavelength is 400–800 nm and the periodic boundary conditions cover the three-dimensional structure model. For the extinction cross-section of a single Li or Au nanoparticle, the Total-Field Scattered-Field (TFSF) is used as a light source, and the boundary condition is a perfect absorption layer. Extinction cross-section is defined as the sum of the scattering and absorption cross-section. The background refractive index is set to 1.4 for representing the liquid electrolyte, and the material data of Li, Au, W, and SiO_2 are all derived from Palik data. The thickness of W and SiO_2 is set to 120 nm and 500 nm. For the reflectance of multiple particles of Li and Au, we used scripts to generate randomly distributed Li or Au nanoparticles with different diameters. The reflectance can be obtained by a vertical incidence of 400–800 nm in a plane wave and a mesh size of 3 μm × 3 μm × 3 μm with the monitor recording.

4.2 Battery fabrication

The battery with an optical window meets the conditions for visible light transmission. The three important parts of preparing a planar battery are the conductive substrate (negative electrode) for lithium metal deposition, the lithium source (positive electrode), and the electrolyte for lithium-ion migration. The details for the negative electrode are seen in the ESI in Fig. S2.† The battery is divided into three layers, the upper layer is quartz glass, the lower layer is the negative electrode of the battery prepared above, and the middle is filled with electrolytes. The cathode electrode of $LiFePO_4$ is glued with conductive copper adhesive and fixed on the other side of the lower SiO_2; for another thing, the anode electrode is led out with conductive copper adhesive as a wire connecting the external circuit. The space around the battery is sealed by UV-curing resin. The electrolyte is 1 M lithium bis(trifluoromethanesulfonyl)imide dissolved in 1,3-dioxolane : dimethoxyethane (1 : 1 volume ratio) with 1 wt% $LiNO_3$ (DodoChem Corporation). Battery fabrication must be carried out in a glovebox. Disassembling the battery is finished by cutting off the copper glue, lifting the upper cover plate (quartz glass sheet), and cleaning in DME solvent in a time of 5 s in a glovebox with an Ar atmosphere. Then the samples are removed in a sealed tank and quickly transferred to the SEM chamber for characterization.

4.3 Characterization

An optical microscope, a spectrometer (PG2000 Pro EX), and an electrochemical workstation (Biologic SP-20) jointly support *in situ* reflectance measurements. The dynamic reflectance spectrum is selected to test the W area on the anode electrode of the planar battery with the electrolyte package used as the reference sample for measuring the light source. Lithium metal particles are deposited and stripped by applying constant current on the electrochemical workstation. At the same time, optical software is used to collect the reflectance spectrum during charging and discharging. For *ex situ* characterization of the lithium morphology, the battery after cycling was opened in an Ar filled glovebox. The electrode in the sealed tank was transferred to the SEM vacuum chamber.

Data availability

Data for this article, including graphs and tables, are available at *Nanoscale Advances* at DOI: **https://doi.org/10.1039/D4NA00950A**.

Author contributions

Huiling Yu: conceptualization, investigation, methodology, experiment, software, data curation, visualization, discussion, and writing – original draft preparation, review, and editing, supervision. The author has read and agreed to the published version of the manuscript.

Conflicts of interest

The author has no conflict to declare.

Acknowledgements

This work was supported by the National Natural Science Foundation of China (No. 51925204, 52381260325), Carbon Peaking and Carbon Neutrality Science and Technology Innovation Fund of Jiangsu Province (BK20220035), Major Research Plan of the National Natural Science Foundation of China (No. 92262305), and National Key Research and Development Program of China (No. 2022YFA1404704). I acknowledge the micro-fabrication center of the National Laboratory of Solid State Microstructures (NLSSM) for technical support.

Notes and references

1 H. A. Atwater and A. Polman, *Nat. Mater.*, 2010, **9**, 205–213.
2 D. D. Song, K. H. Zhang, M. D. Qian, Y. F. Liu, X. H. Wu and K. Yu, *Nanomaterials*, 2022, **13**, 91.
3 R. S. M, L. H. Zhu, R. W. Peng, R. H. Fan, X. R. Huang and M. Wang, *Opt. Express*, 2013, **21**, A313–A323.
4 K. T. Lee, C. Ji and L. J. Guo, *Appl. Phys. Lett.*, 2016, **108**, 031107.
5 C. Yang, C. Ji, W. Shen, K. T. Lee, Y. Zhang, X. Liu and L. J. Guo, *ACS Photonics*, 2016, **3**, 590–596.
6 T. D. Dao, K. Chen, S. Ishii, A. Ohi, T. Nabatame, M. Kitajima and T. Nagao, *ACS Photonics*, 2015, **2**, 964–970.
7 J. A. Mason, S. Smith and D. Wasserman, *Appl. Phys. Lett.*, 2011, **98**, 241105.
8 J. Wu, *Opt. Commun.*, 2016, **365**, 93–98.
9 S. Linic, P. Christopher and D. B. Ingram, *Nat. Mater.*, 2011, **10**, 911–921.
10 N. Liu, M. Mesch, T. Weiss, M. Hentschel and H. Giessen, *Nano Lett.*, 2010, **10**, 2342–2348.
11 Y. Cheng, X. S. Mao, C. Wu, L. Wu and R. Gong, *Opt. Mater.*, 2016, **53**, 195–200.
12 Z. Wei, Y. Jiang, S. Zhang, X. Zhu and Q. Li, *IEEE Photonics J.*, 2022, **14**, 1–6.
13 D. Schurig, J. J. Mock, B. J. Justice, S. A. Cummer, J. B. Pendry, A. F. Starr and D. R. Smith, *Science*, 2006, **314**, 977–980.
14 X. P. Li, Y. Y. Chen, R. Zhu and G. L. Huang, *Mech. Syst. Signal Process.*, 2020, **149**, 107324.
15 J. F. Wang, S. B. Qu, X. Zhuo and M. Hua, *J. Phys. D Appl. Phys.*, 2011, **44**, 315501.
16 M. Kadic, T. Bückmann, R. Schittny and M. Wegener, *Philos. Trans. A Math. Phys. Eng. Sci.*, 2015, **373**, 20140357.
17 D. Wu, C. Liu, Y. Liu, L. Yu, Z. Yu, L. Chen, R. Ma and H. Ye, *Opt. Lett.*, 2017, **42**, 450–453.
18 Y. Cui, K. H. Fung, J. Xu, H. Ma, Y. Jin, S. He and N. X. Fang, *Nano Lett.*, 2012, **12**, 1443–1447.
19 Q. Liang, T. Wang, Z. Lu, Q. Sun, Y. Fu and W. Yu, *Adv. Opt. Mater.*, 2013, **1**, 43–49.
20 J. Dai, M. Qiu and M. Yan, *J. Opt.*, 2014, **16**, 30–39.
21 M. Eskandari, A. Habibzadeh-Sharif and M. Nazari, *Iran. J. Sci. Technol.*, 2023, **3**, 47.
22 Y. Li, C. J. Lin, K. Q. Li, C. Chi and B. L. Huang, *Nano Lett.*, 2022, **22**, 5659–5666.
23 P. Zhu and L. Jay Guo, *Appl. Phys. Lett.*, 2012, **101**, 241116–241120.
24 P. Hosseini, C. D. Wright and H. Bhaskaran, *Nature*, 2014, **511**, 206–211.
25 R. Dao, X. Kong, H. F. Zhang and X. Tian, *Plasmonics*, 2019, **15**, 169–175.
26 J. He, M. Zhang, S. Shu, Y. Yan and M. Wang, *Opt. Express*, 2020, **28**, 37590–37599.
27 T. Cao, C. W. Wei, R. E. Simpson, L. Zhang and M. J. Cryan, *Sci. Rep.*, 2014, **4**, 3955.
28 G. H. Rui, C. C. Ding, B. Gu, Q. Q. Gan, Q. W. Zhan and Y. P. Cui, *J. Opt.*, 2020, **22**, 30–39.
29 L. Ju, F. G. Castaldi, T. K. D. Ko, Y. Zhang and P. J. P. S. Wang, *Nat. Nanotechnol.*, 2011, **6**, 630–634.
30 A. N. Grigorenko, M. Polini and K. S. Novoselov, *Nat. Photonics*, 2012, **6**, 749–758.
31 M. Toma, U. Jonas, A. Mateescu, W. Knoll and J. Dostalek, *J. Phys. Chem. C*, 2013, **117**, 11705–11712.
32 Y. Ma, H. Wang, J. Wu, Y. Xu, L. Huang and L. Zhang, *ACS Appl. Mater. Interfaces*, 2019, **11**, 22754–22760.
33 M. L. Tseng, H. G. M. Yu, T. B. Chen, C. H. Huang and Y. H. Chen, *Nano Lett.*, 2017, **17**, 6034–6039.
34 P. Gutruf, J. W. H. Lee, W. Zhang, Y. X. Wang and C. P. Wong, *ACS Nano*, 2016, **10**, 133–141.
35 J. Hao, J. Wang, X. Liu, W. J. Padilla, L. Zhou and M. Qiu, *Appl. Phys. Lett.*, 2010, **96**, 251104–251107.
36 S. Butun and K. Aydin, *Opt. Express*, 2014, **22**, 19457–19468.
37 A. Vora, J. Gwamuri, N. Pala, A. Kulkarni, J. M. Pearce and D. O. Guney, *Sci. Rep.*, 2014, **4**, 4901.
38 S. K. Patel, S. Charola, J. Parmar and M. Ladumor, *Mater. Res. Express*, 2019, **6**, 086213.
39 C. Wang, D. Zhao, C. R. Grice, W. Liao, Y. Yu, A. Cimaroli, N. Shrestha, P. J. Roland, J. Chen, Z. Yu, P. Liu, N. Cheng, R. J. Ellingson, X. Zhao and Y. Yan, *J. Mater. Chem. A*, 2016, **4**, 12080–12087.
40 Y. Zhou, Z. Qin, Z. Liang, D. Meng, H. Xu, D. R. Smith and Y. Liu, *Light Sci. Appl.*, 2021, **10**, 138.
41 Y. Wang, J. Yu, Y. F. Mao, J. Chen, S. Wang, H. Z. Chen, Y. Zhang, S. Y. Wang, X. Chen, T. Li, L. Zhou, R. M. Ma, S. Zhu, W. Cai and J. Zhu, *Nature*, 2020, **581**, 401–405.
42 D. He, C. Su, C. Zhao, G. Yan, Z. Zhao and W. Mai, *Chem. Eng. J.*, 2022, **438**, 135469.
43 Y. Jin, J. Liang, S. Wu, Y. Zhang, L. Zhou, Q. J. Wang, H. Liu and J. Zhu, *Adv. Mater.*, 2020, **32**, e2000058.
44 Y. Jin, L. Zhou, J. Y. Yu, J. Liang, W. S. Cai, H. G. Zhang, S. N. Zhu and J. Zhu, *Proc. Natl. Acad. Sci. U. S. A.*, 2018, **115**, 11168–11173.
45 J. Liang, Y. Jin, H. L. Yu, X. J. Chen, L. Zhou, P. C. Huo, Y. Zhang, H. Y. Ma, Y. Jiang, B. Zhu, T. Xu, H. Liu, S. N. Zhu and J. Zhu, *Natl. Sci. Rev.*, 2023, **10**, nwac120.
46 C. Cui, H. Yang, C. Zeng, S. W. Gui, J. N. Liang, P. Xiao, S. H. Wang, G. X. Huang, M. T. Hu, T. Y. Zhai and H. Q. Li, *Sci. Adv.*, 2022, **8**, eadd2000.